Available online at www.sciencedirect.com
SCIENCE DIRECT®
Journal of Nuclear Materials 342 (2005) 48–62
journal of nuclear materials
www.elsevier.com/locate/jnucmat

Dual phase MgO–ZrO_2 ceramics for use in LWR inert matrix fuel ☆

P.G. Medvedev *, S.M. Frank, T.P. O'Holleran, M.K. Meyer

Argonne National Laboratory West, Idaho Falls, ID 83404-2528, USA

Received 8 December 2004; accepted 7 March 2005

Abstract

To address the low thermal conductivity of the ZrO_2-based inert matrix fuel and the instability in water of the MgO-based inert matrix fuel, the dual-phase MgO–ZrO_2 ceramics are proposed as a matrix for light water reactor fuel for actinide transmutation and Pu burning. It is envisioned that in a dual-phase system MgO will act as efficient heat conductor while ZrO_2 will provide protection from the coolant attack. This paper describes results of fabrication, characterization and hydration testing of MgO–ZrO_2 ceramics containing 30–70 wt% of MgO.

PACS: 28.41.Bm; 81.05.Je; 81.05.Mh; 28.41.Kw

1. Introduction

Inert Matrix Fuel (IMF) is a type of nuclear reactor fuel that consists of a neutron-transparent matrix and a fissile phase that is either dissolved in the matrix or incorporated as macroscopic inclusions. The matrix plays a crucial role of diluting the fissile phase to the volumetric concentrations required by reactor control considerations, the same role U-238 plays in conventional low enriched uranium (LEU) or mixed uranium–plutonium oxide (MOX) fuel. The key difference is that replacing U-238 with a neutron-transparent matrix eliminates plutonium breeding as a result of neutron capture.

IMF technology is believed to have a great potential to improve the efficiency of in-reactor disposal of plutonium, and provide opportunities for disposal of neptunium, americium and curium. The latter group of elements is also known as minor actinides. Estimates [1] have shown that if plutonium is used as a fissile phase, at least 90% of it will be destroyed. Therefore, IMF irradiation campaign intakes proliferation-prone nuclear material with very high radiotoxicity (half-life of several thousands of years) and yields a valuable commodity such as energy and short-lived radioactive waste that can be managed considerably more easily than the original stream of plutonium and actinides.

No other technology is currently available to target at the same time the radiotoxicity and proliferation risks of the surplus nuclear material. The mixed oxide

☆ Work supported by the Advanced Fuel Cycle Initiative of the US Department of Energy under contract no. W-31-109-ENG-38.

* Corresponding author. Tel.: +1 208 533 7199; fax: +1 208 533 7863.

E-mail addresses: pavel.medvedev@anlw.anl.gov, medvedev@inel.gov (P.G. Medvedev).

0022-3115/$ - see front matter © 2005 Elsevier B.V. All rights reserved.
doi:10.1016/j.jnucmat.2005.03.017

fuel path currently accepted for in-reactor plutonium disposition does make surplus plutonium unattractive for weapons. However the issue of nuclear waste from MOX irradiations remains unresolved. At the present time the IMF burning combined with nuclear waste transmutation are the industry's only prospects for a waste-free nuclear cycle.

Technical feasibility of the IMF technology relies heavily on material properties of the matrix. The matrix must meet the following criteria:

- high thermal conductivity,
- compatibility with reactor materials,
- high radiation resistance,
- low neutron absorption cross-section,
- meet acceptance criteria for either direct disposal or reprocessing.

Materials research, development and evaluation are currently a top priority in strengthening a case for burning plutonium and minor actinides using IMF. The research in the field is expected to continue until a product that meets general criteria outlined above is developed and licensed for use in LWR by a nuclear regulatory body.

The present study was supported by the Advanced Fuel Cycle Initiative of the US Department of Energy and was performed in the Nuclear Technology Division of Argonne National Laboratory (ANL). Inspired by favorable physical properties of MgO [2] and positive irradiation experience of MgO-based fuels [3–5], ANL decided to further investigate the possibility of use of this material in light water reactors. Recognizing that inability of MgO to withstand hydration attack by LWR coolant is the factor limiting use of MgO in LWR, this work is dedicated to development, characterization and assessment of an MgO-based material compatible with LWR coolant. Although the LWR fuel is protected by Zircaloy cladding, it is important for the fuel to retain its integrity in case of the contact with coolant in an event of the cladding failure.

A more detailed description of this project can be found elsewhere [6].

2. Development and characterization of magnesia-based ceramics with improved hydration resistance

2.1. Preliminary considerations

To develop magnesia-based ceramics with improved hydration resistance, the phenomenon of magnesia hydration and possible strategies to disrupt hydration investigated by reviewing the relevant literature and conducting a set of preliminary experiments. The findings of these research efforts are discussed herein.

2.1.1. Observations of magnesia hydration

Hydration of magnesia in hydrothermal conditions is catastrophic and results in a complete conversion to hydroxide. Neither single crystals, nor polycrystals of near theoretical density are immune. Kitamura et al. [7] has demonstrated that both are destroyed within 10–20 h in saturated water vapor at 200 °C. These observations related to magnesia ceramics were confirmed in this work by conducting hydration tests on magnesia ceramics. Immersion-type hydration tests were performed in boiling water at atmospheric pressure and in a water-filled pressure vessel at 300 °C. Effect of the exposure to the boiling water was investigated by visual observation, optical microscopy (Trinocular Stereoscopic Zoom Microscope Nikon SMZ-2T), and scanning electron microscopy (SEM, Zeiss DSM960A). Fig. 1 illustrates severe degradation of a magnesia ceramic pellet (density 2.99 g/cm^3) caused by exposure of the pellet to the boiling water. Profuse cracking and swelling caused by hydration are difficult to overlook.

Optical microscopy of a polished and thermally etched surface of magnesia ceramic (density 3.45 g/cm^3), exposed to the boiling water, revealed that cracks develop within an hour of exposure (Fig. 2(a)). Cracks propagating from the surface of the pellet were found on the polished and thermally etched cross-section of magnesia ceramic briefly exposed to the water at 300 °C (Fig. 2(b)). SEM provided additional evidence (Fig. 2(c) and (d)) of the degradation believed to be caused by hydration. These observations, once again, rule out safe use of pure magnesia as an inert matrix for LWR fuels.

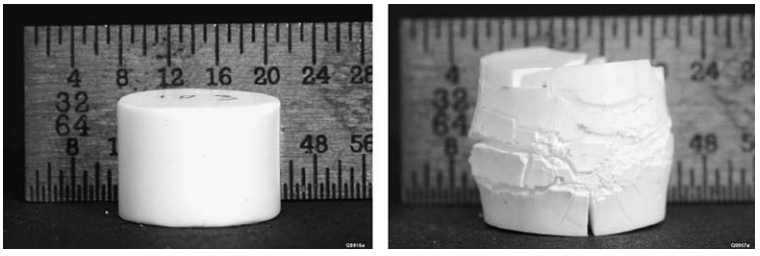

Fig. 1. As manufactured magnesia ceramic pellet (left) and a magnesia ceramic pellet after a 3-h exposure to the boiling water (right).

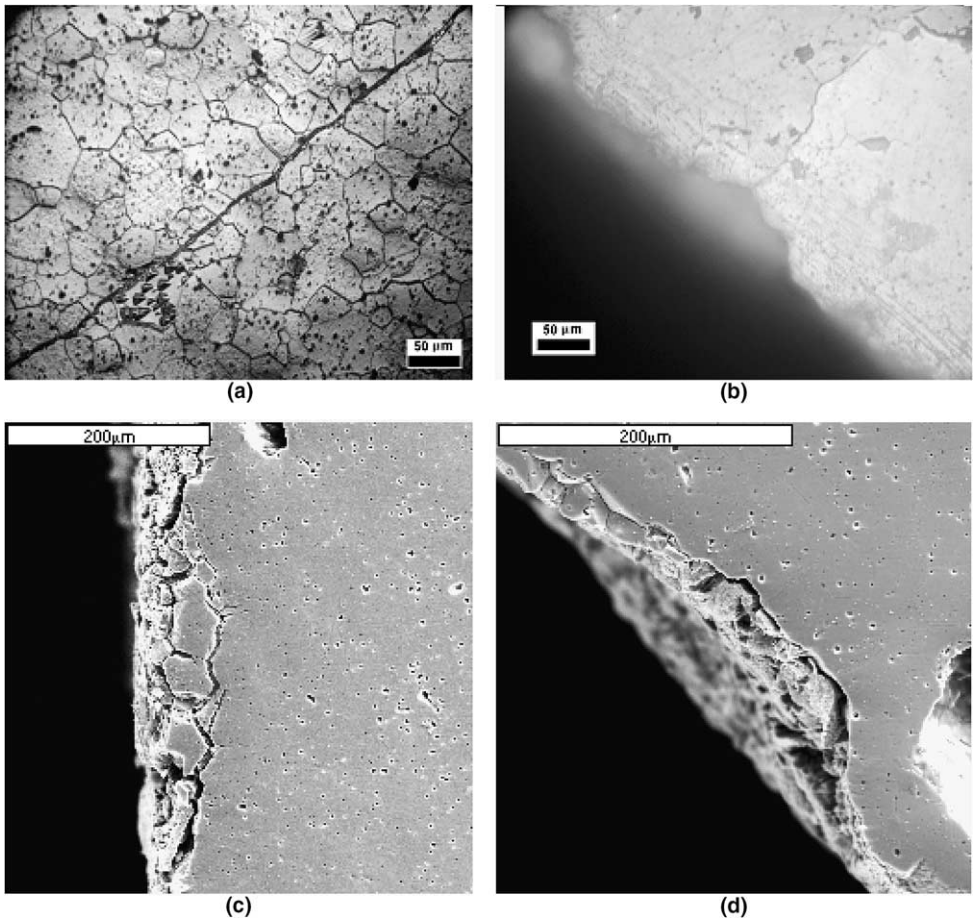

Fig. 2. Optical microscopy (a, b) and SEM images (c, d) illustrating degradation of magnesia ceramics exposed to the boiling water (a) and 300 °C water (b–d).

2.1.2. Nature of the hydration problem and possible solutions

Kitamura et al. [7] proposed the following hydration mechanism for magnesia polycrystals. The hydration attack begins on the grain boundaries near the surface of polycrystalline magnesia. It causes grain boundary destruction, disintegration of the polycrystal, first into finer particles, then into single crystals, with consequent hydration of single crystals. The initial stage of the process is characterized by hydration of exposed grain surfaces and grain boundaries. The chemical reaction between magnesia and water is accompanied by a volume increase of 117%. As a result, the hydration product, forming on the grain boundaries, exerts stresses on the neighboring grains. With the buildup of the hydration product on the grain boundaries, the stresses become large enough to initiate cracking. The cracks serve as pathways for the water exposing more magnesia available for hydration. Finally, the grain boundaries of the first layer of grains are destroyed, and the first layer of grains is detached from the monolith. The process then repeats itself until the entire polycrystalline monolith is powderized, i.e. reduced to individual grains. Hydration of individual grains separated from the monolith continues at a slower rate until all magnesia is converted to hydroxide.

The following measures are likely to be effective in reducing the hydration rate:

- Surface coating which acts as a physical barrier separating water from magnesia;
- Use of additives resulting in a formation of a hydration-resistant grain boundary phase, solid solution, or a multiphase system.

Coating individual fuel pellets to protect them from hydration is not viable due to the cost considerations. Furthermore, radiation induced swelling, cracking due to thermal gradients, and fission gas release associated with fuel operation would constantly challenge the

integrity of the coating. Therefore, the use of additives is a more promising proposal, given the nature of the intended application. It is known, that some oxide additives have long been used to control the sintering kinetics, microstructure and toughness of magnesia ceramics [8,9]. However, their effect on hydration has never been fully investigated. This study will address this aspect.

2.1.3. Selection of an additive to improve hydration resistance of magnesia

The initial search of candidate additives was focused on classic refractory materials: zirconia (ZrO_2), alumina (Al_2O_3), silica (SiO_2), and spinel ($MgAl_2O_4$). Members of this list have high melting temperatures, low neutron absorption cross-sections, and are highly hydration-resistant. It is understood, that this list is far from being exhaustive. Other materials, such as NiO, BeO, ZrC, SiC, AlN, and $ZrO_2 \cdot SiO_2$ may be effective additives as well. However, recognizing the budget and time limitations of this project, only materials included in the first list were given further consideration.

To select an additive from the list of candidates discussed above, a set of quick preliminary experiments was conducted. Binary ceramic composites containing magnesia and one of the following: zirconia, alumina, silica, and spinel; were fabricated using conventional pressing and sintering techniques. Resulting pellets were tested for hydration resistance in boiling water. Among tested combinations only magnesia–zirconia composites containing up to 50 mol.% of zirconia have shown an improvement in hydration resistance. Based on these results, zirconia was selected as an additive to improve hydration resistance of magnesia. Further research was focused solely on magnesia–zirconia ceramics.

2.2. Experimental procedure

Once the zirconia was selected as an additive to improve hydration resistance of magnesia ceramics, a procedure to fabricate magnesia ceramics doped with zirconia was developed. This fabrication procedure and the analytical techniques utilized to characterize the microstructure of the final product are presented in this section.

2.2.1. Magnesia–zirconia ceramic fabrication

Magnesia–zirconia ceramic composites were fabricated using conventional pressing and sintering techniques. Magnesium oxide (item M-1017, lot X25111, typically 99.95% pure) was procured from Cerac Incorporated (Milwakee, WI). Magnesium zirconium oxide (stock 12343, lot C01E, 99.7% metals basis) supplied by Alfa Aesar (Ward Hill, MA) was used as a source of zirconia. When choosing the source of zirconia, the preference was given to magnesium zirconium oxide rather then pure zirconium oxide. This saved some effort required for producing a homogeneous mixture of the two. Recognizing that LWR fuels often contain burnable neutron poisons, erbium oxide (lot C25H, 99.9% metals basis), Johnson Matthey Electronics (Ward Hill, MA), was added to some compositions.

Pre-weighed amounts of magnesia, erbia, and magnesium zirconium oxide powders were combined with water in a beaker. The weight of water was approximately three times greater than the weight of the powders combined. The water and powder mixture were stirred using a magnetic stirring bar for 6 h. The slurry was dried in air at 80 °C for 5 h. The resulting powder was transferred into an alumina crucible and heat-treated at 1000 °C for 5 h in a high temperature tube furnace (model F59348CM-75, Barnstead International, Dubuque, IA). Upon cool-down, zinc stearate (Fisher Scientific Fair Lawn, NJ, Z-78-4, lot 871095, UPS grade) in the amount of 1% by weight was mixed into the powder using a mortar and a pestle. The powder was then pressed into pellets with a force of 44.45 kN using a cylindrical die of 12.72 mm diameter. Resulting pellets were ground into powder using mortar and pestle. The powder was passed through a sieve with an aperture size of 212 μm (ASTM-E11 #70). The mixture was pressed again into pellets with a force of 13.34 kN using a cylindrical die of 12.72 mm diameter. The pellets were placed into alumina crucibles and sintered in air for 7.5 h at 1700 °C in a high temperature tube furnace (model F59348CM-75, Barnstead International, Dubuque, IA). The pellets were cooled with the furnace after sintering.

2.2.2. Characterization

Sintered pellets were subjected to optical microscopy (Trinocular Stereoscopic Zoom Microscope Nikon SMZ-2T), scanning electron microscopy (SEM, Zeiss DSM960A), energy dispersive X-ray analysis (EDS, Oxford Instruments, Freemont, CA), X-ray diffraction analysis (XRD, Scintag X1), pycnometric density measurements (Ultapycnometer-1000, Quantachrome Inc, Boyton Beach, Fl), and immersion density measurements. Green density of the pressed pellets was derived from their weight and linear dimensions measured using an electronic caliper.

2.3. Results and discussion

2.3.1. Ceramic fabrication

Ceramics of three binary and three ternary compositions were fabricated. The binary compositions were as follows:

- 30 wt% MgO 70 wt% ZrO_2, further referred as 30/70;
- 40 wt% MgO 60 wt% ZrO_2, further referred as 40/60;

- 50 wt% MgO 50 wt% ZrO_2, further referred as 50/50;
- 60 wt% MgO 40 wt% ZrO_2, further referred as 60/40.

The ternary compositions:

- 37.2 wt% MgO 55.8 wt% ZrO_2 7 wt% Er_2O_3, further referred as 40/60-Er;
- 46.5 wt% MgO 46.5 wt% ZrO_2 7 wt% Er_2O_3, further referred as 50/50-Er;
- 55.8 wt% MgO 37.2 wt% ZrO_2 7 wt% Er_2O_3, further referred as 60/40-Er.

Fabrication of ceramics of several compositions was undertaken in order to provide further opportunity to explore possible compositional dependence of the microstructure and properties of the final product. Photographs of ceramic pellets are shown in Fig. 3. The pellet on the left is light pink due to erbia doping.

2.3.2. Scanning electron microscopy and energy dispersive X-ray analysis

Typical microstructure observed for the binary magnesia–zirconia compositions is shown in Fig. 4. Two phases comprise the ceramic microstructure. The dark phase is magnesia and the light phase is a magnesia–zirconia solid solution. In this system the microstructure is obviously driven by the ratio between batched amounts of the initial components. The 60/40 composition appeared as a dispersion of zirconia in the magnesia phase, while the 40/60 composition was clearly a dispersion of magnesia in the zirconia phase. The 50/50 composition manifested itself as a combination of two interpenetrating phases.

The microstructures observed in the ternary erbia–magnesia–zirconia compositions were similar to those of binary compositions. Two phases comprised the ceramic microstructure: magnesia and erbia–magnesia–zirconia solid solution. As in the binary system described above, the microstructure of the ternary system was driven by the ratio between batched amounts of the initial components.

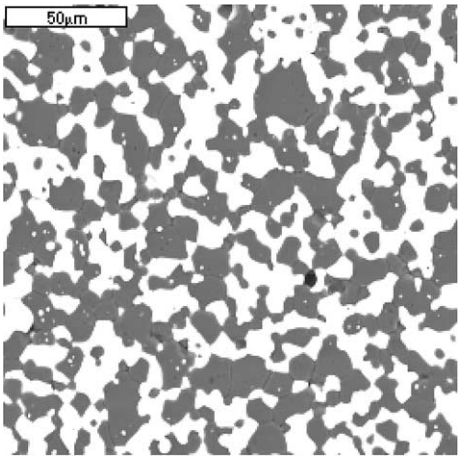

Fig. 4. SEM image of the 50/50 ceramic.

High magnification scanning electron microscopy revealed presence of nano-sized substructure on the surface of zirconia grains in the magnesia–zirconia sample (Fig. 5(a)). This substructure was not detected in the erbia-doped sample (Fig. 5(b)).

The amount of magnesium present in the zirconia phase was determined by the standardless energy dispersive (EDS) X-ray spectrometry. The analysis of each sample was performed by measuring the concentrations of magnesium and zirconium in 15 locations within zirconia grains. The resulting ratios between magnesium and zirconium atomic concentrations are shown in Table 1. These ratios represent the average of the meaningful measurements. The standard deviation is also included. The Zr/Mg atomic ratios for binary compositions shown in Table 1 are in good agreement with the published phase diagram for MgO–ZrO_2. According to the latter, the solubility of MgO in ZrO_2 at 1700 °C is approximately 16% M, which is equivalent to the Zr/Mg atomic ratio of 5.25.

Using a similar approach, the magnesia phase was analyzed for the presence of zirconium and erbium. The analysis of each sample was performed by measuring the concentrations of magnesium, zirconium and

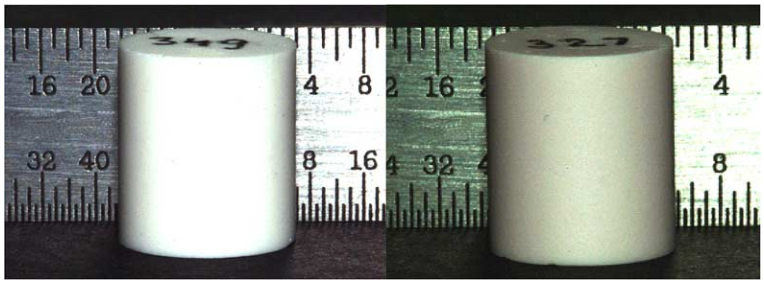

Fig. 3. As-sintered magnesia–zirconia ceramic (60/40, left) and magnesia–zirconia ceramic doped with erbia (50/50-Er, right).

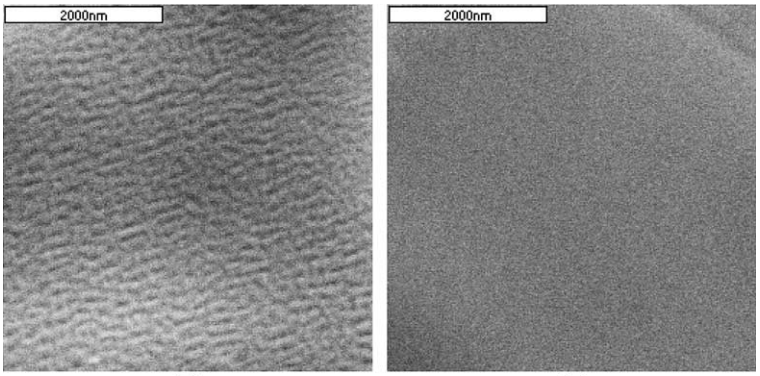

Fig. 5. Nano-sized substructure on the surface of a zirconia grain in the magnesia–zirconia sample (a) shown in contrast with a smooth surface of a zirconia grain in the erbia-doped magnesia–zirconia sample (b).

Table 1
Composition of the zirconia phase

Sample	Zr/Mg ratio of atomic concentrations	Solid solution composition	Solid solution theoretical density (g/cm^3)
40/60	5.35 ± 0.58	$Mg_{0.158}Zr_{0.842}O_{1.842}$	5.56
50/50	5.24 ± 0.60	$Mg_{0.160}Zr_{0.840}O_{1.840}$	5.55
60/40	4.81 ± 0.60	$Mg_{0.172}Zr_{0.828}O_{1.828}$	5.51
40/60-Er	5.50 ± 0.74	$Er_{0.067}Mg_{0.143}Zr_{0.789}O_{1.823}$	5.78
50/50-Er	5.78 ± 0.82	$Er_{0.082}Mg_{0.135}Zr_{0.783}O_{1.824}$	5.87
60/40-Er	5.63 ± 0.90	$Er_{0.099}Mg_{0.136}Zr_{0.765}O_{1.815}$	5.95

erbium in 5 locations within magnesia grains. No zirconium or erbium was detected in magnesia grains.

Since the EDS analysis detected no erbium presence in the magnesia phase, the amount of erbium present in zirconia grains was determined from the batched amounts of erbium and zirconium oxides, assuming that all added erbium oxide has completely dissolved in zirconia. The EDS analysis to determine erbium content in the zirconia phase was attempted as well. However, the measured values were higher than expected due to the matrix effects explained by the higher atomic number of erbium as compared to other constituents of the ceramic.

The amount of oxygen shown in Table 1 was determined from the known stoichiometry of the metal-to-oxygen ratio of the oxides. The following oxidation states were used: Mg^{2+}, Zr^{4+}, Er^{3+}.

2.3.3. X-ray diffraction analysis

X-ray diffraction analysis of samples was performed on binary and ternary compositions. First, the analysis was carried out on ~1.5 mm thick discs cut from as-sintered pellets. After completion of the analysis, the discs were ground in a mortar and passed through a sieve with an aperture of 45 μm. The resulting powder was re-analyzed. The XRD spectra from sintered and cut monolithic samples were found to be identical to the respective powder patterns, thus it was concluded that no phase transformation was induced by grinding. The XRD results presented herein are for the powdered samples.

Refinement of the XRD patterns was performed with DMS/NT data acquisition and analysis software. Refinement included background and k-alpha-2 stripping, peak-finding, matching library files with the data, peak profile fitting, peak indexing and lattice parameter determination. Phases detected in the analyzed samples are listed in Table 2. Typical raw XRD spectrum is shown in Fig. 6. Evidently, the transition from one composition to another does not result in a change of the phase make up of the ceramics. The only difference between the XRD patterns was in the relative peak intensity, which is caused by the difference in relative amounts of magnesia and zirconia phases. This implies that any possible compositional property dependence in these ceramics will be driven solely by the ratio between the cubic zirconia and cubic magnesia phases, not by a phase transformation. These observations and conclusions also apply to the ternary compositions.

Results of the XRD analysis relative to the behavior of erbia dopant in the magnesia–zirconia system were consistent with the EDS findings. Because no other erbium-containing phases were detected by XRD, erbia had to have dissolved in either magnesia or zirconia

Table 2
Phase identified by X-ray diffraction analysis

Sample	Identified phases			Lattice parameter (Å)	
	ZrO_2-cubic	ZrO_2-monoclinic	MgO-cubic	ZrO_2 cubic phase	MgO phase
40/60	Yes	Trace	Yes	5.0782	4.2100
50/50	Yes	Trace	Yes	5.0782	4.2089
60/40	Yes	Trace	Yes	5.0763	4.2103
40/60-Er	Yes	No	Yes	5.1042	4.2112
50/50-Er	Yes	No	Yes	5.0999	4.2102
60/40-Er	Yes	No	Yes	5.0969	4.2100

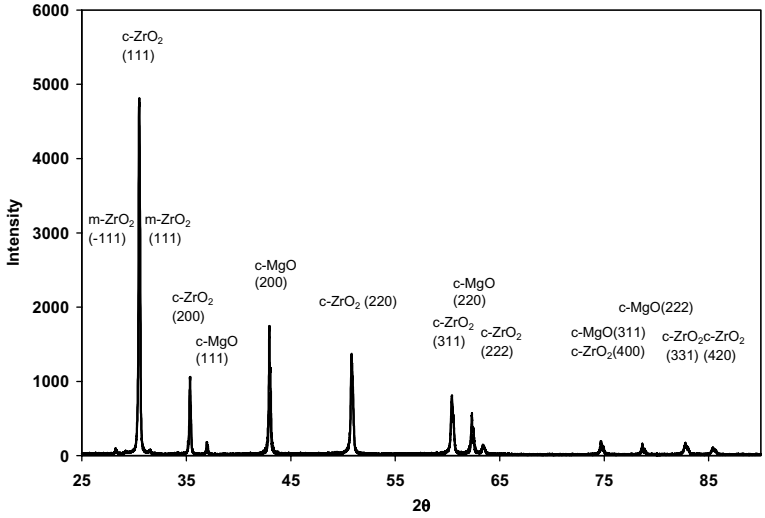

Fig. 6. Typical XRD spectrum. MgO–ZrO_2 ceramic composition is 50/50.

phases. Since the pattern from magnesia phase matched very well the corresponding library pattern, and the magnesia lattice parameter matched the corresponding library value (4.2112 Å), the magnesia phase can be considered practically pure. On the other hand, the zirconia pattern exhibited a notable peak shift to the left, when Er was added to the system (Fig. 7). The shift was explained by the expansion of the zirconia unit cells caused by substitution of zirconium ions with larger erbium ions. Furthermore, the trace amounts of monoclinic zirconia present in binary magnesia–zirconia compositions were not detected in the erbia doped samples, likely due to stabilization of zirconia by erbia. Based on these observations it was concluded that erbia has fully dissolved in the zirconia phase and formed a ternary erbia–magnesia–zirconia solid solution.

2.3.4. Density

Results of the density measurements are shown in Table 3. The theoretical density of the composites was calculated from the theoretical densities of the constituent phases: magnesia- and zirconia-based solid solution. The theoretical density of magnesia is known to be 3.58 g/cm^3. The theoretical density of the zirconia-based solid solutions was calculated from their crystallographic unit cell weight and volume. The crystallographic unit cell weight was determined from the stoichiometry of the solid solutions, and the unit cell volume was determined from the lattice parameter measured by XRD. The resulting theoretical density values of the zirconia-based solid solutions are given in Table 1. The relative amount of the phases in the composites was determined from the mass balance.

2.4. Simulation of dispersion-type fuel fabrication

To imitate fabrication of the dispersed fuel, 0.1 mm diameter zirconia microspheres simulating fissile inclusions were added prior to sintering to the ceramic compositions under investigation. The microspheres (lot 1000168) were obtained from Tosoh Corporation (Tokyo, Japan). The purpose of this experiment was to

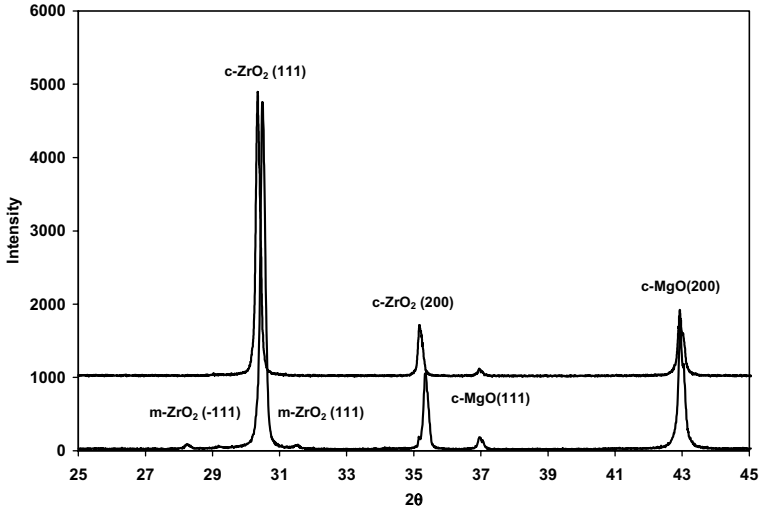

Fig. 7. Shift of the zirconia phase reflections caused by Er doping. Top spectrum: 50/50-Er composition, bottom: 50/50.

Table 3
Results of the density measurements

Sample	Density (g/cm^3)			
	Green	Pycnometric	Immersion	Theoretical
40/60	2.68	4.61	4.61	4.63
50/50	2.45	4.40	4.39	4.41
60/40	2.25	4.18	4.19	4.20
40/60-Er	2.78	4.81	4.76	4.79
50/50-Er	2.55	4.56	4.54	4.58
60/40-Er	2.40	4.35	4.33	4.38
MgO	1.84	3.57	3.45	3.58

demonstrate that the microspheres can be sintered into the ceramic, and a high-quality crack-free product can be obtained. Optical micrograph of the ceramic containing the microspheres are shown in Fig. 8. The image reveals that the microsphere is fully integrated into the surrounding matrix. Absence of cracks is an evidence of good thermal and mechanical compatibility between of the microsphere and the ceramic.

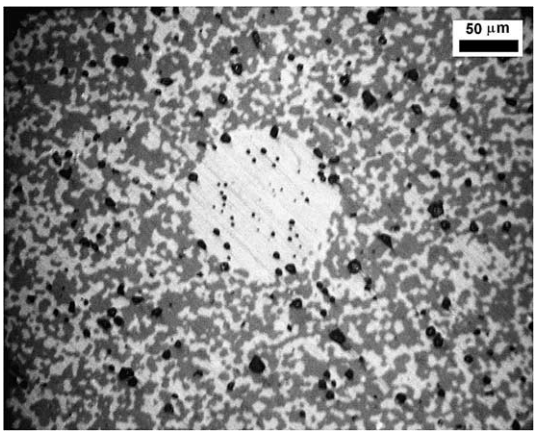

Fig. 8. Optical micrograph of the ceramic containing microspheres. MgO–ZrO_2 matrix composition is 50/50.

3. Investigation of hydration resistance

3.1. Experimental procedure

The purpose of hydration testing was threefold: to assess the mass loss of the magnesia–zirconia ceramics in hydrothermal conditions, to determine the effect of the zirconia content on the mass loss, and to investigate the mechanism behind improved hydration resistance. The particulars of hydration tests are as follows. As-sintered ceramic pellets were exposed to static de-ionized water at 300 °C for the periods of up to 30 days. The tests were performed in a commercial 316 stainless steel 2-l pressure vessel (model 4622, Parr Instrument Company, Moline, Illinois), rated for operation at a maximum pressure of 1900 psi at 350 °C. The pressure vessel was equipped with a pressure relief valve set at 1700 psi, a 2100 psi rupture disk, a pressure gauge, an inlet/outlet valve, a heating mantle, and a temperature controller with two thermocouples. During the operation the thermocouples resided in a specially designed thermowell protruding into the reaction volume.

As-sintered ceramic pellets were placed into the pressure vessel filled with 1 l of de-ionized water. The vessel was closed, positioned in the heating mantle and the thermocouples were inserted into the thermowell. The temperature controller was set at 300 °C. A heating time of 1 h was required for the water temperature to reach

this setting. After that the test continued without further operator intervention until the desired exposure time was attained.

Periodically, the heat to the pressure vessel was shut off, the vessel was allowed to cool, and samples were removed, rinsed with de-ionized water, visually inspected, dried for 5 h at 80 °C, and weighed. Some samples were photographed, analyzed by optical microscopy (Trinocular Stereoscopic Zoom Microscope Nikon SMZ-2T), SEM (Zeiss DSM960A), EDS (Oxford Instruments, Freemont, CA), and XRD (Scintag X1). After the samples were placed back into the vessel, the vessel was refilled with fresh water and the test was resumed. The typical frequency of such shut-downs was once every 5 days.

The tests were intended to simulate the exposure of an IMF pellet to the reactor coolant in an event of a fuel pin failure and consequent ingress of reactor coolant into the failed fuel pin. It is recognized that an ideal simulation of such event would involve a dynamic test where the water is allowed to flow through the test volume. However, the water solubility of the phases comprising the ceramic under investigation is minimal, and the degradation mechanism is not driven by dissolution, but by hydration of magnesia. Thus, it was concluded that no 'poisoning' of water would occur during long-term hydration tests. Here the term 'poisoning' implies saturation of water by dissolved species turning the water non-reactive towards the ceramic. Due to these considerations, the static tests were chosen as a low cost and robust alternative to the dynamic tests. For the same reasons, the tests were performed on multiple samples simultaneously, rather then on one sample per run. A test-to-test consistency of the ratio of the sample surface area to the liquid volume, normally required in situation when sample dissolution is present, was unnecessary here. A typical surface area to the liquid volume ratio in these tests was up to 3 m^{-1}. This involves testing up to six ceramic pellets per run, with each pellet having a surface area of 0.5 cm^2 in an autoclave filled with 1 l of water.

3.2. Results and discussion

3.2.1. Effect of zirconia content on the mass loss due to hydration

As mentioned earlier, the pellet mass loss was used as a quantitative indicator of the extent of hydration. The Normalized Mass Loss (NML) was determined from measured mass loss according to the following equation:

$$\mathrm{NML}(t) = \frac{m_i - m(t)}{A_i} \quad (1)$$

where m_i – sample mass before the exposure, g; $m(t)$ – sample mass after the exposure at time t, g; A_i – initial sample surface area, cm^2.

The plot of NML versus the elapsed time in hours observed at the temperature of 300 °C is shown in Fig. 9. The plot represents the tests conducted for three samples of each composition, except the 30/70 composition for which only two samples were tested. The data points on the plot represent the mass loss measured during periodic shut-downs.

The plot (Fig. 9) shows good reproducibility of the NML between different samples of the same compositions. The data scatter observed here is due to occasional chipping of the pellets during tests. The chipping was likely caused by inhomogeneity of the samples and possibly by contamination of the surface layers of the pellets by the furnace insulation debris during sintering.

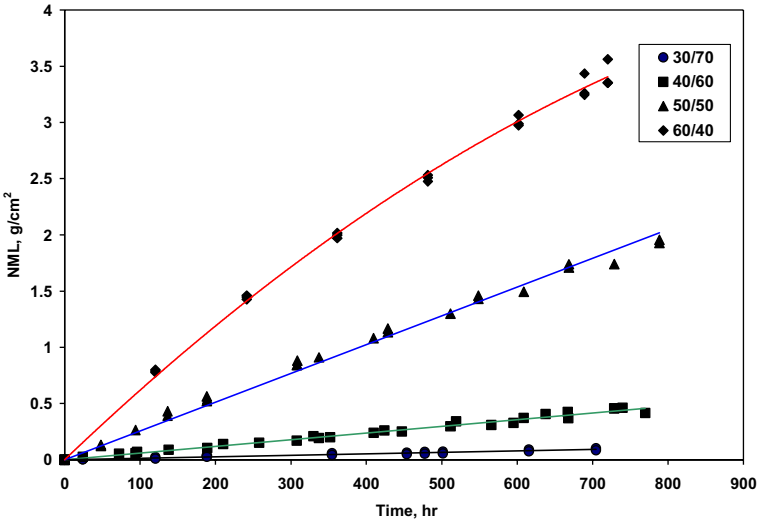

Fig. 9. Normalized ceramic mass loss due to hydration versus the elapsed time.

The normalized mass loss rate (NMLR) can be readily determined from the slope of the curves in Fig. 9. The NMLR is shown in Fig. 10 as a function of zirconia content. The Arrhenius-type trendline in Fig. 10 follows the equation:

$$\mathrm{NMLR} = 1.6569 \exp\left(-\frac{2c_{\mathrm{Zr}}}{15}\right) \quad (2)$$

where NMLR is the normalized mass loss rate in grams per square centimeter of the ceramic surface per hour, and c_{Zr} is zirconia content in weight percent.

Erbia doping had a negative effect on hydration resistance. The NMLR for the 50/50-Er composition was 0.003669 g/cm^2/h while the NMLR for the 50/50 composition was 0.002559 g/cm^2/h.

3.2.2. Observation of the hydrated microstructures and hydration mechanism

Photographs of magnesia–zirconia ceramics after exposure to water at 300 °C for 720 h are shown in Fig. 11. As evident from Fig. 11, the integrity of the pellets is preserved. However, some roughness is obvious in both pellets as well as chipping in the case of the erbia-doped sample. Nevertheless, these images establish a remarkable contrast with Fig. 1, in which severe hydration-induced degradation of pure magnesia ceramics is illustrated.

To understand the mechanism behind the improved hydration resistance in magnesia–zirconia ceramics, several hydrated pellets were examined by SEM and XRD. SEM was conducted with an objective to locate the hydration product, and to determine the extent of degradation on the microscopic scale. XRD was performed to identify the crystallographic phases present in the hydrated samples.

An SEM image of a magnesia–zirconia ceramic surface after exposure to the de-ionized water at 300 °C for 700 h is shown in Fig. 12. The bright phase shown in Fig. 12 is a magnesia–zirconia solid solution. The dark phase contains both MgO and $Mg(OH)_2$. This

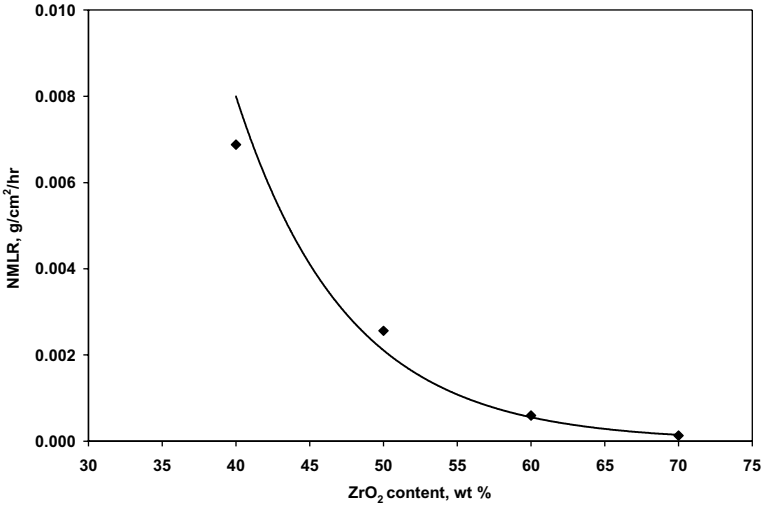

Fig. 10. Normalized mass loss rate as a function of zirconia content.

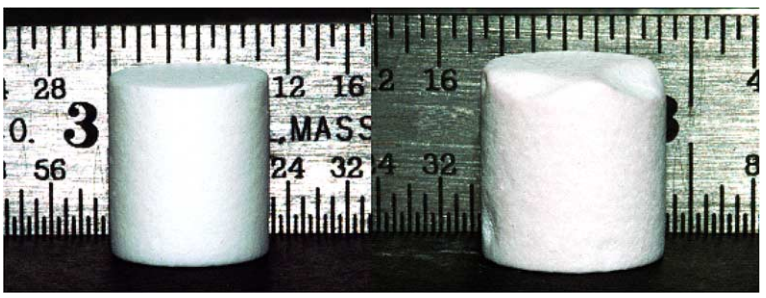

Fig. 11. Magnesia–zirconia (60/40) ceramic (left) and magnesia–zirconia ceramic doped with erbia (50/50-Er) (right) after 720 h of exposure to the water at 300 °C.

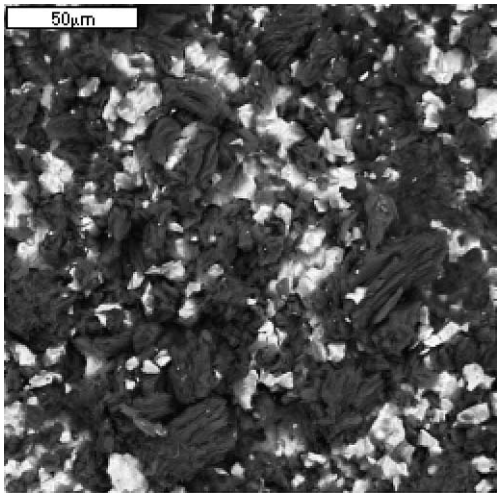

Fig. 12. Surface of the 50/50 ceramic after 700 h exposure to water at 300 °C. White phase: ZrO_2–MgO(ss); grey phase: $Mg(OH)_2$ + MgO.

phase was analyzed by conducting point-by-point EDS to determine the atomic ratio between magnesium and oxygen. EDS revealed that the dark phase contained approximately 1.5 oxygen atoms per 1 magnesium atom. Because MgO contains 1 oxygen atom per 1 magnesium atom, and $Mg(OH)_2$ contains 2 oxygen atoms per 1 magnesium atom, the dark phase observed in Fig. 12 is likely MgO with the hydration product $Mg(OH)_2$ deposited on its surface. Because the penetration depth of the electron probe has exceeded the thickness of the $Mg(OH)_2$ layer, the resulting EDS spectrum represents a sum of the spectra produced by the surface $Mg(OH)_2$ layer and the underlying MgO layer.

To evaluate the extent of hydration in relation to the volume of the ceramic pellet rather than its surface, a pellet, previously exposed to the de-ionized water at 300 °C for 700 h, was cut with a high speed diamond saw, polished and thermally etched. The pellet's cross-section was then examined by SEM. The results of this examination are shown in Fig. 13. Incomplete and missing MgO grains present on the pellet's edge were interpreted as the signs of a hydration attack. The arrows in Fig. 13 point to such sites. As evident from Fig. 13, only magnesia grains located on the surface of the pellet and supposedly exposed to the water show signs of degradation. Other grains appear intact. Thorough examination of the remainder of the cross-section was unable to detect any hydration damage beyond the surface layer of the grains.

Earlier it was shown that in the case of pure magnesia ceramics the degradation quickly propagates inside the sample due to the hydration induced cracking that provides pathways for the water. Therefore, absence of hydration-induced cracks in magnesia–zirconia ceramics is a key difference in microstructure of the hydrated pure magnesia ceramics and the dual-phase magnesia–zirconia ceramics.

XRD analysis of a hydrated ceramic was first performed on a monolithic sample. The sample was prepared by cutting a disc from an as-sintered pellet. The disc was then exposed to water at 300 °C for 240 h. After exposure the disc was dried in 80 °C air for 5 h and subjected to X-ray diffraction analysis. After completion of the analysis the disc was ground in a mortar and passed through a sieve with an aperture of 45 μm. The resulting powder was re-analyzed. The superposition of the XRD patterns from the monolithic and powdered sample is shown in Fig. 14. In addition to the phases characteristic for the as-sintered ceramic (cubic magnesia–zirconia solid solution and cubic magnesia), the hexagonal magnesium hydroxide $Mg(OH)_2$ was found in the monolithic sample. However, the peaks related to magnesium hydroxide were missing from the pattern collected from the powdered sample. This is likely due to the fact that magnesium hydroxide was present as a thin layer on the surface of a hydrated monolithic sample. Grinding

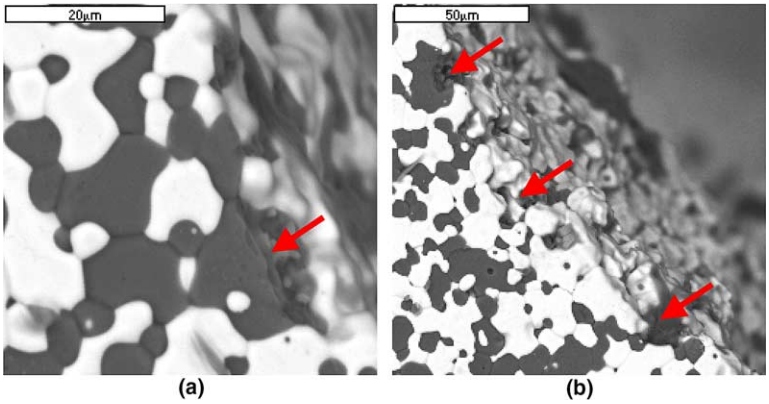

Fig. 13. Edge of polished and thermally etched cross-section of the 40/60 ceramic after 700 h exposure to water at 300 °C.

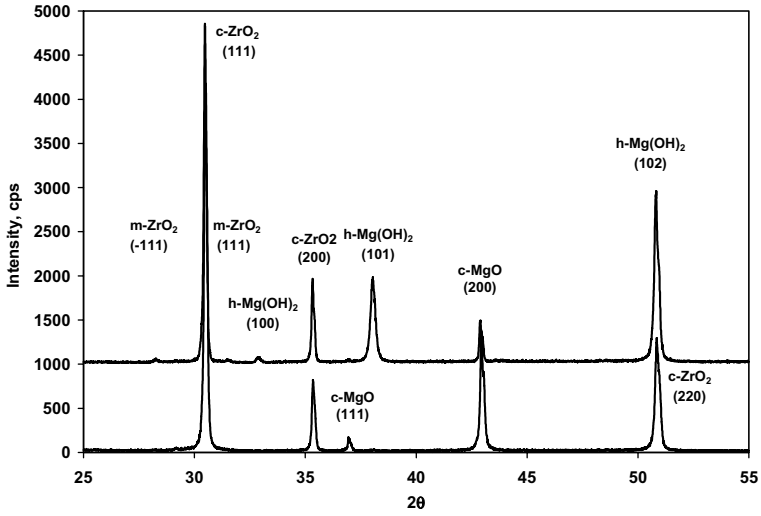

Fig. 14. Superposition of the XRD patterns from the monolithic and powdered hydrated sample (50/50). Top spectrum: monolithic sample, bottom: powdered sample.

caused dilution of magnesium hydroxide by the bulk of the sample driving the magnesium hydroxide concentration below the detection limit. These observations are consistent with the results of the SEM analysis of the hydrated microstructures discussed earlier in this section. Both SEM and XRD detect the hydration product magnesium hydroxide, but only on the surface of the ceramic.

While some of the hydration product was detected on the surface of the samples, the bulk of it sloughed from the samples and deposited on the bottom of the pressure vessel. This residue was collected, dried for 5 h at 80 °C and subjected to the XRD analysis. The analysis of the residue revealed that it consists of two phases: cubic magnesia–zirconia solid solution and hexagonal magnesium hydroxide. The superposition of this pattern with the pattern from an as-sintered powdered ceramic is shown in Fig. 15.

The superposition points to the absence of magnesia but presence of magnesium hydroxide in the residue, which indicates that magnesia lost by the sample is completely converted to hydroxide. The pattern for the cubic

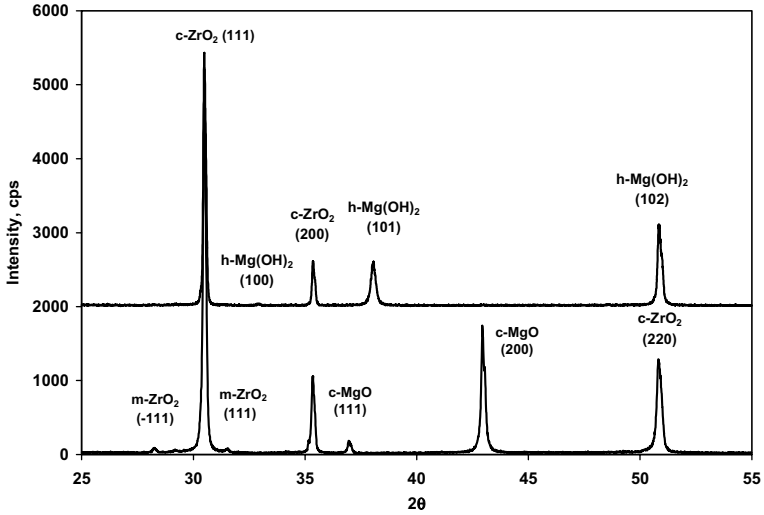

Fig. 15. Superposition of the XRD patterns from the residue collected from the bottom of the pressure vessel and from as-sintered powdered ceramic. Top spectrum: residue, bottom: as-sintered powdered ceramic.

magnesia–zirconia solid solution in the residue is identical to that in the as-sintered sample. Furthermore, because no shift of zirconia peaks is observed between the two patterns, the composition of the solid solution is unaffected by hydration. No leaching of magnesium occurred from the solid solution. The most important conclusion stemming from the XRD analysis of the residue is that degradation of the magnesia–zirconia ceramics is solely due to the hydration of the magnesia phase. The loss of the cubic magnesia–zirconia solid solution phase occurs because the neighboring magnesia grains are destroyed, and the solid solution grains are no longer attached to the monolith.

Based on these considerations, a schematic diagram of the hydration process shown in Fig. 16 was developed. The hydration begins on the surface and on the grain boundaries of magnesia grains (Fig. 16(a)). As in the case with pure magnesia ceramic, the stresses do arise on the grain boundaries due to the volume increase associated with the hydration reaction. These stresses are shown as the arrows perpendicular to grain boundaries. However, the stresses in this case are not sufficient to initiate cracking of the ceramic. This assertion is based on the SEM observations that showed absence of cracks and confinement of the degradation to the surface layer of the grains, and on the XRD results that indirectly indicated that the hydration product is present as a thin layer on the surface of the ceramics. With the cracks absent, the hydration is limited to the magnesia grains on the surface (Fig. 16(b)). Once they are consumed, the next layer of grains is attacked (Fig. 16(c)). The hydration product in the form of fine particulate is removed from the site of reaction by convective water movement and deposited on the bottom of the pressure vessel. Finally, enough magnesia is consumed so that zirconia grains belonging to the first layer loose the bond with the monolith and are deposited on the bottom of the pressure vessel (Fig. 16(d)). The process then repeats itself.

The key factor behind the improvement of the hydration in magnesia–zirconia ceramics as compared to pure magnesia ceramics is its ability to withstand the hydration induced cracking. The other significant factor is reduction of the surface area of the magnesia phase due to addition of the insoluble zirconia phase.

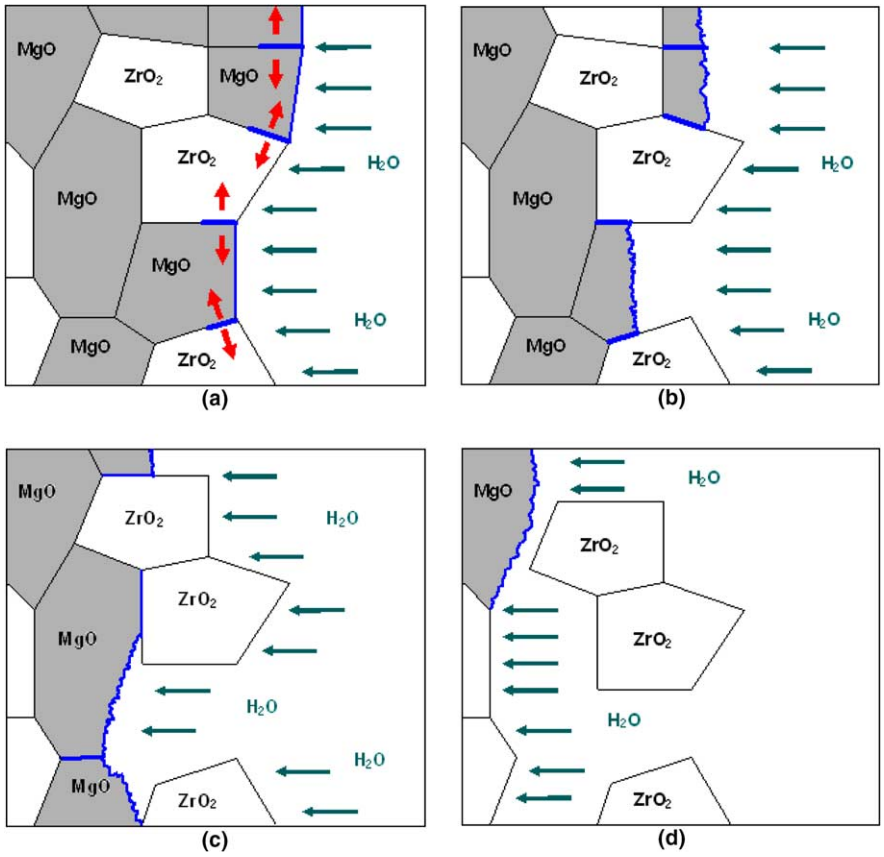

Fig. 16. Schematic of the hydration process of the magnesia–zirconia ceramics.

3.2.3. Effect of the boron presence in the water on hydration resistance

Presence of boron in the water had a dramatic positive effect on the hydration resistance. At 300 °C the NMRL for the 50/50 composition was 0.00005667 g/cm^2/h in the 13 000 ppm aqueous solution of the boric acid containing trace amounts of lithium hydroxide. This is 45 times less than the NMRL measured for the same ceramic in the de-ionized water. Furthermore, the mass loss exhibited saturation with time, as evident from Fig. 17. Saturation of mass loss with time is a key difference between the behavior in borated and de-ionized water. This suggests that the reaction in borated water is likely self-limiting and results in the passivation of magnesia.

Explanation of the positive effect of boron on the hydration resistance was found by conducting XRD analysis of the surface of the ceramic pellet previously exposed to the 13 000 ppm aqueous solution of the boric acid at 300 °C. The corresponding XRD pattern is shown in Fig. 18. Besides magnesia and magnesia–zirconia solid solution phases, the magnesium borate hydroxide $Mg(OH)BO_2$ was identified in the sample. Magnesium hydroxide, typically observed in samples exposed to the de-ionized water, was not detected in the sample exposed to the borated water. Based on these

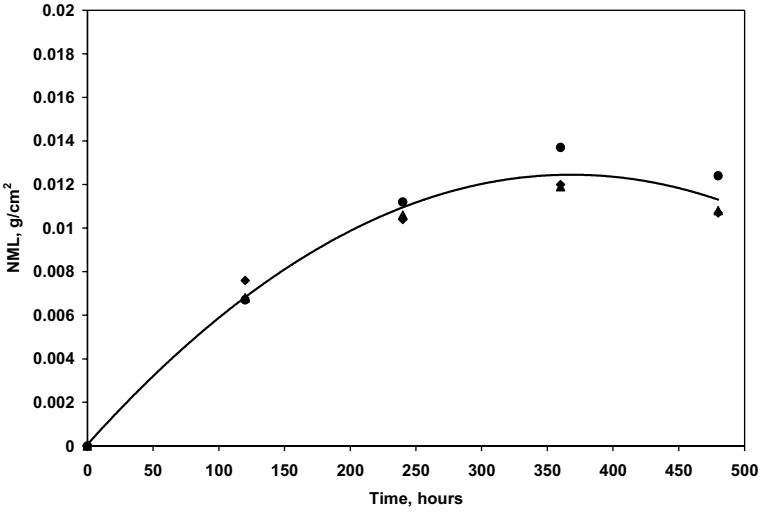

Fig. 17. Saturation with time of the sample mass loss exhibited in the 13 000 ppm borated water.

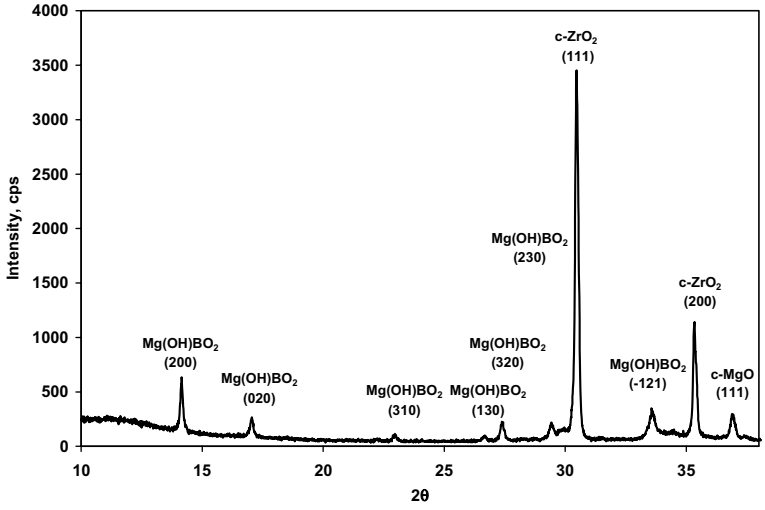

Fig. 18. XRD pattern of the surface of the ceramic pellet exposed to the 13 000 ppm aqueous solution of the boric acid at 300 °C.

results it was concluded that in the presence of the boric acid the reaction of magnesia with water with formation of magnesium hydroxide is suppressed. Instead, the following reaction takes place:

$$MgO + H_3BO_3 \rightarrow Mg(OH)BO_2 \downarrow + H_2O$$

Therefore, the difference in the behavior of the ceramics in de-ionized and borated water is due to the different chemical reaction that takes place during exposure.

It is recognized, that in a LWR the boron concentration is expected to vary from 0 ppm to 4400 ppm depending on the reactor power and burnup [10]. Here the concentration of 4400 ppm of boron is equivalent to the 25 198 ppm of boric acid. Thus, the value of 13 000 ppm used in this work represents a median value. A more detailed investigation of the boron effect on the hydration resistance, particularly at different boron concentrations, was beyond the scope of this work. However, the results shown here indicate that presence of boron in the reactor coolant should be viewed as an advantage in addressing the fuel safety implications of the hydration issue.

4. Conclusions

The main outcome of this work is the development of a principally new inert matrix for LWR fuel: dual-phase magnesia–zirconia ceramics. The concept for use of this composite material in LWR was developed with the intent to capitalize on the known advantages of the composite's constituents: magnesia and zirconia. It is expected that magnesia will bring high thermal conductivity while zirconia will provide protection from the LWR coolant attack.

The product was fabricated by conventional pressing and sintering techniques of the oxide mixture. Product characterization performed using SEM, EDS, and XRD established presence of two major phases: cubic magnesia–zirconia solid solution and cubic magnesia. Erbia doping intended to simulate addition of the burnable poison, resulted in a complete dissolution of erbia in the zirconia-based solid solution without significant rejection of magnesia from the said solid solution. No erbia was detected in the magnesia phase. The dopant behavior in magnesia–zirconia system is exceptionally favorable, because by preferentially dissolving in zirconia phase, the dopant does not contaminate the highly thermally conductive magnesia phase.

When it came to chemical interaction with simulated reactor coolant, the product featured exponential decrease of the mass loss due to hydration with an increase of zirconia content. The normalized mass loss rates measured in static 300 °C de-ionized water for the magnesia–zirconia ceramics containing 40, 50, 60, and 70 wt% of zirconia were 0.00688, 0.00256, 0.000595, 0.000131 g/cm^2/h respectively. The presence of boron in the water had a dramatic positive effect on the hydration resistance. At 300 °C the normalized mass loss rates for the composition containing 50 wt% of zirconia was 0.00005667 g/cm^2/h in the 13 000 ppm aqueous solution of the boric acid.

A closer look on the microstructure and composition of the product previously exposed to the de-ionized water, helped to understand the mechanism behind the improved hydration resistance and to establish the contrast between pure magnesia ceramics and magnesia–zirconia ceramics. SEM and XRD analyses suggested that as in the case of pure magnesia, the mass loss of magnesia–zirconia ceramics occurred due to hydration of the magnesia phase. However, presence of zirconia in the system tended to eliminate the hydration-induced cracking typical for pure magnesia ceramics and responsible for its catastrophic degradation in hydrothermal conditions. With the elimination of cracking, the hydration occurs on the surface of the ceramics, and proceeds in a layer-by-layer mode.

Acknowledgements

Dr Jue is gratefully acknowledged for helpful discussions on the subject of ceramic development and characterization. Sincere thanks to Mr Knighton, Mr DeGiuli, and Mr Simpson for manufacturing and troubleshooting the ceramic fabrication and testing equipment, and to Mr Hahn and Mr Olsen for photography services.

References

[1] K.E. Sickafus, R.J. Hanrahan, K.J. McClellan, J.N. Mitchell, C.J. Wetteland, D.P. Butt, P. Chodak, K.B. Ramsey, T.H. Blair, K. Chidester, H. Matzke, K. Yasuda, R.A. Verrall, N. Yu, Am. Ceram. Soc. Bull. 78 (1999) 69.
[2] H. Kleykamp, J. Nucl. Mater. 275 (1999) 1.
[3] M.D. Freshley, D.F. Carroll, Trans. Am. Nucl. Soc. 6 (1963) 396.
[4] E.A.C. Neeft, K. Bakker, R.P.C. Schram, R. Conrad, R.J.M. Konings, J. Nucl. Mater. 320 (2003) 106.
[5] N. Chauvin, T. Albiol, R. Mazoyer, J. Noirot, D. Lespiaux, J.C. Dumas, C. Weinberg, J.C. Ménard, J.P. Ottaviani, J. Nucl. Mater. 274 (1999) 91.
[6] P.G. Medvedev, Development of dual-phase magnesia–zirconia ceramics for light water reactor inert matrix fuel, Dissertation, Texas A&M University, 2004.
[7] A. Kitamura et al., Taikabutsu Overseas 16 (1996) 3.
[8] W. Nelson, I.B. Cutler, J. Am. Ceram. Soc. 41 (1958) 406.
[9] T.C. Yuan et al., J. Mater. Sci. 24 (1989) 3855.
[10] C.C. Lin, Radiochemistry in Nuclear Power Reactors, National Academy Press, Washington, 1996, p. 1.